JOURNAL OF GEOPHYSICAL RESEARCH, VOL. 106, NO. A8, PAGES 15,609–15,619, AUGUST 1, 2001

Transient development of magnetohydrodynamic wave mode conversion layers

J. De Keyser and V. Čadež

Belgian Institute for Space Aeronomy, Brussels, Belgium

Abstract. We study the transmission, reflection, and absorption of ultralow frequency waves at density nonuniformities in low beta plasmas, such as plasma structures in the solar corona, inhomogeneities in the solar wind, and, at times, in the magnetopause. We simulate the time-dependent interaction of a monochromatic magnetohydrodynamic (MHD) wave with a planar plasma transition layer aligned with the magnetic field. When the incident wave front reaches the initially unperturbed transition layer, a resonant sheet starts to develop within a thin layer where the conditions for resonant MHD wave mode conversion are satisfied. In this sheet the wave amplitude is found to grow exponentially until a saturation level is reached due to dissipative effects. Dissipation controls the thickness of the sheet, the saturation level, and the time needed to reach the saturation regime. The resonantly absorbed energy, however, is essentially independent of the dissipation coefficient. The simulations are carried out in the context of linear resistive low beta magnetohydrodynamics. The simulation results are important for the case of the magnetopause as the enhanced wave amplitudes found inside the transition could promote diffusive mass transport across the layer.

1. Introduction

It is well known that a dissipationless plasma, that contains a field-aligned sheath across which the plasma and magnetic field characteristics change, can support (1) magnetohydrodynamic (MHD) waves that propagate across the sheath and (2) waves that propagate parallel to it, also called "local modes." While the former can be of any MHD wave mode (fast, Alfvén, or slow), the latter can only be Alfvén or slow waves. Such a one-dimensional nonuniform plasma configuration allows for a phenomenon known as resonant MHD mode conversion. This happens when an incident magnetoacoustic MHD wave, after entering the nonuniform plasma region, encounters a location where the condition for wave phase matching with local MHD modes is satisfied. Propagation of these linear local modes is governed by local dispersion relations; these waves are bounded to individual magnetic planes in which the plasma parameters do not vary. There is a coupling between the incident wave and the local eigenmodes on that particular magnetic surface. Consequently, the local mode starts resonating with the incoming wave and the wave amplitude grows at the location of the resonance. Either the local Alfvén or the local slow magnetoacoustic waves can be excited. The resonant wave amplitude is limited by dissipation and by nonlinearity. Eventually, dissipative effects cause the resonant local waves to lose their energy on account of plasma heating within the resonant layer. The net effect is that a fraction of the energy carried by the incident wave is resonantly absorbed.

In space physics, MHD wave mode conversion has been invoked in the context of the Earth's magnetosphere and the solar corona. One application is the theory of magnetospheric pulsations [*Southwood*, 1974; *Mann et al.*, 1995]. An important application is the interaction of magnetosheath waves with the magnetopause [*McKenzie*, 1970]. The resonantly amplified ultralow frequency (ULF) fluctuation level at the magnetopause [*Perraut et al.*, 1979; *Rezeau et al.*, 1989] may promote diffusive mass and energy transport into the magnetosphere [*Belmont et al.*, 1995; *De Keyser et al.*, 1999; *De Keyser*, 2000]. Solar physics and solar wind applications include the problem of heating of the corona by waves or by footpoint motions of field lines anchored in the photosphere [*Poedts et al.*, 1989; *Goossens and Hollweg*, 1993; *Čadež and Ballester*, 1996; *Čadež et al.*, 1997].

The main subject of this paper is the time evolution of linear MHD mode conversion in a resistive and low beta plasma. We consider a planar slab transition between two uniform plasma regions. The magnetic field is constant, unidirectional, and parallel to the slab. This configuration is representative, for instance, of the low-shear subsolar magnetopause. The problem of mode conversion has been studied in the past by means of Fourier-Laplace transforms looking either at eigenmodes and quasi-modes of the MHD equations or at solutions of driven systems assuming a periodic external driver. The present paper, however, addresses systems with a nonperiodic driver by solving the resistive MHD equations as a full initial value/boundary value problem. We focus on lateral driving of mode conversion lay-

Paper number 2001JA900045.
0148-0227/01/2001JA900045$09.00

ers in the magnetopause by incident magnetosheath waves; we do not consider direct driving of the field lines. Also, we numerically integrate across the resonant layer rather than using the classical connection formulae [*Sakurai et al.*, 1991; *Goossens et al.*, 1995; *Goossens and Ruderman*, 1995]. Our simulations reveal an exponential growth of the wave amplitude in a newly forming resonant sheet, as well as its saturation due to dissipation. These simulations of the transient development of resonant sheets are important as an illustration of the mode conversion mechanism in its own right, but also in view of the intermittent nature of driver waves in the space environment, such as magnetosheath waves arriving at the magnetopause [*Anderson et al.*, 1982]. In particular, the enhanced magnetic field fluctuations that we find here as a result of resonant mode conversion can promote mass transport across the magnetopause. Such a mass transport is not modeled here (a kinetic rather than a fluid approach would be more appropriate to do so), but wave-particle interactions and the associated diffusive mass transport [*Treumann et al.*, 1995; *Sibeck et al.*, 1999], for instance, are strongly enhanced if the magnetic fluctuation level is enhanced by an order of magnitude, as suggested by the simulations in this paper.

2. Magnetohydrodynamic Description

We consider a typical subsolar magnetopause configuration with x being the gradient direction of changes in plasma properties meaning that the plasma slab is parallel to the y,z plane. Thermal effects are ignored (low beta assumption). Gravitation is not considered. Let ρ denote the mass density, $\boldsymbol{v}$ denote the bulk velocity, $\boldsymbol{j}$ denote the electric current density, and $\boldsymbol{B}$ and $\boldsymbol{E}$ denote the magnetic and electric fields. The initial unperturbed state is a static equilibrium ($\boldsymbol{v}^{(0)} \equiv \boldsymbol{0}$) in which the magnetic field $B^{(0)} = 50$ nT is constant (in order to satisfy pressure balance) and unidirectional along the z axis. The plasma structure is that of a tangential discontinuity separating magnetosphere (msph) and magnetosheath (msh), with a density variation

$$\rho^{(0)}(x) = \rho_{\mathrm{msph}}\mathcal{G}(x/D) + \rho_{\mathrm{msh}}\mathcal{G}(-x/D),$$

where $\mathcal{G}(x/D) = \frac{1}{2}\,\mathrm{erfc}\,(x/D)$ (erfc is the complementary error function) which allows a smooth transition with a half-width $D = 300$ km [*Berchem and Russell*, 1982], and where $\rho_{\mathrm{msph}}/m = 1\ \mathrm{cm}^{-3}$ and $\rho_{\mathrm{msh}}/m = 20\ \mathrm{cm}^{-3}$ (m is the ion+electron mass). This equilibrium is depicted in Figure 1. The Alfvén speed $v_A = B^{(0)}/\sqrt{\mu_0\rho^{(0)}}$ varies from 244 km s^{-1} in the magnetosheath to 1091 km s^{-1} in the magnetosphere (Figure 1b). The one-dimensional approximation becomes invalid for distances larger than a few Earth radii, when the magnetosheath flow away from the subsolar point and the curvature of the magnetopause can no longer be ignored. The low beta continuity and momentum equations are

$$\frac{\partial\rho}{\partial t} + \nabla\cdot(\rho\boldsymbol{v}) = 0, \tag{1}$$

$$\frac{\partial\rho\boldsymbol{v}}{\partial t} + \nabla\cdot\left[\rho\boldsymbol{v}\boldsymbol{v} + \frac{B^2}{2\mu_0}\boldsymbol{I} - \frac{1}{\mu_0}\boldsymbol{B}\boldsymbol{B}\right] = \boldsymbol{0}. \tag{2}$$

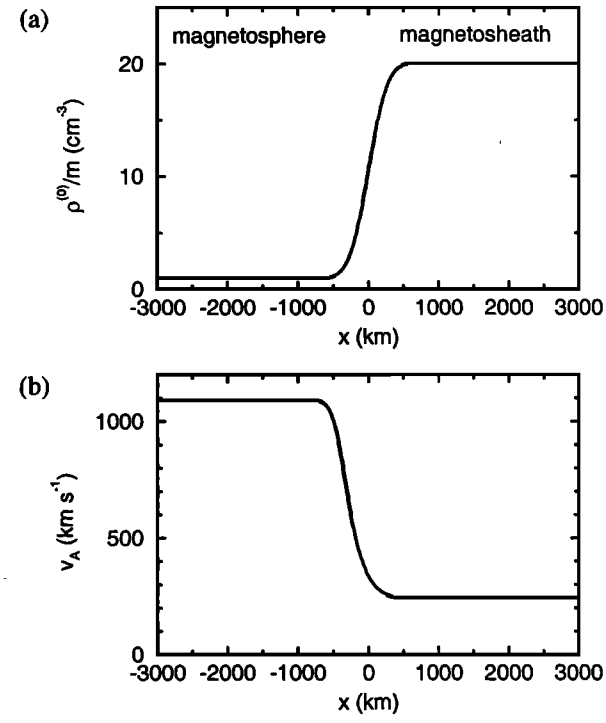

Figure 1. Equilibrium low-shear subsolar magnetopause configuration. For low beta conditions the magnetic field is constant and unidirectional, so that the transition is fully determined by (a) the density profile with a characteristic half width of 300 km, which is responsible for (b) the Alfvén speed variation across the layer. The magnetosphere in this and subsequent plots is always to the left, and the magnetosheath is to the right.

where $\boldsymbol{I}$ is the unit tensor. The generalized Ohm's law is

$$\boldsymbol{E} + \boldsymbol{v}\times\boldsymbol{B} = \eta\mu_0\boldsymbol{j}, \tag{3}$$

with $\mu_0\eta$ being the resistivity. Maxwell's equations become

$$\nabla\times\boldsymbol{B} = \mu_0\boldsymbol{j}, \tag{4}$$

$$\frac{\partial\boldsymbol{B}}{\partial t} + \nabla\times\boldsymbol{E} = \boldsymbol{0}, \tag{5}$$

$$\nabla\cdot\boldsymbol{B} = 0. \tag{6}$$

The solution is assumed to consist of a one-dimensional equilibrium $\boldsymbol{q}^{(0)}(x)$ upon which small-amplitude waves are superimposed: $\boldsymbol{q}(x,y,z,t) = \boldsymbol{q}^{(0)}(x) + \boldsymbol{q}^{(1)}(x,y,z,t)$. It is implicitly understood that the perturbations do not affect the equilibrium. While Ohmic dissipation will heat up the plasma, the solutions remain valid only as long as the low beta approximation is justified. Since the plasma resistivity is very small in space plasmas, this imposes an upper time limit on the simulations that is much larger than the timescales of the phenomena considered here. The linearized wave propagation equations can be expressed as

$$\frac{\partial\boldsymbol{q}^{(1)}}{\partial t} + v_A\left(\boldsymbol{A}_x\frac{\partial}{\partial x} + \boldsymbol{A}_y\frac{\partial}{\partial y} + \boldsymbol{A}_z\frac{\partial}{\partial z}\right)\boldsymbol{q}^{(1)} = \eta\boldsymbol{C}\nabla^2\boldsymbol{q}^{(1)}, \tag{7}$$

with $\boldsymbol{q}^{(1)} = [v_x^{(1)}, v_y^{(1)}, B_x^{(1)}, B_y^{(1)}, B_z^{(1)}]$, and where

$$\mathcal{A}_x=\begin{bmatrix} . & . & . & . & b^{-2} \\ . & . & . & . & . \\ . & . & . & . & . \\ . & . & . & . & . \\ b^2 & . & . & . & . \end{bmatrix}, \quad \mathcal{A}_y=\begin{bmatrix} . & . & . & . & . \\ . & . & . & . & b^{-2} \\ . & . & . & . & . \\ . & . & . & . & . \\ . & b^2 & . & . & . \end{bmatrix},$$

$$\mathcal{A}_z=\begin{bmatrix} . & . & -b^{-2} & . & . \\ . & . & . & -b^{-2} & . \\ -b^2 & . & . & . & . \\ . & -b^2 & . & . & . \\ . & . & . & . & . \end{bmatrix}, \quad \mathcal{C}=\begin{bmatrix} . & . & . & . & . \\ . & . & . & . & . \\ . & . & 1 & . & . \\ . & . & . & 1 & . \\ . & . & . & . & 1 \end{bmatrix},$$

and $b^2 = B^{(0)}/v_A$, and where η is the magnetic diffusivity. It should be noted that $v_z^{(1)} \equiv 0$ as the plasma cannot be accelerated along the magnetic field lines: Neither the electric nor the magnetic force have a component along the field line ($\boldsymbol{E}^{(1)} \perp \boldsymbol{B}^{(0)}$) and the thermal pressure is negligible in a low beta plasma.

We will solve the initial value problem for a harmonic perturbation initially occupying only a part of the uniform plasma, located beyond some given distance from the nonuniform slab. Such a step-like harmonic wave enters the solution domain at $t = 0$ and has the following form: $\boldsymbol{q}^{(1)} \propto \exp i(k_x x + k_y y + k_z z - \omega t)$ with circular frequency $\omega = 2\pi f$ and wave vector $\boldsymbol{k} = [k_x, k_y, k_z]$. The wave equations (7) yield the dispersion relation

$$(\omega^2 - k_z^2 v_A^2)(\omega^2 - k^2 v_A^2) = 0$$

in the uniform domain. The first and the second factor correspond to the Alfvén and the fast magnetoacoustic mode, respectively, which are the only two MHD wave modes supported in a uniform low beta plasma. As the wave enters the nonuniform slab, its amplitude remains harmonic in y and z while its x and time dependence have to be computed from (7). In addition to the incident wave, we have to deal with the aforementioned local modes that propagate parallel to the slab. There is no convective flux in the direction perpendicular to the slab associated with such waves; hence $\mathcal{A}_x \partial \boldsymbol{q}^{(1)}/\partial x \equiv \boldsymbol{0}$. This implies that the state variables that contribute to the x flux (v_x and B_z) must be identically zero for the local waves. In the absence of dissipation, (7) takes the form

$$\frac{\partial}{\partial t}\begin{bmatrix} v_y^{(1)} \\ B_y^{(1)} \end{bmatrix} + v_A \begin{bmatrix} . & -b^{-2} \\ -b^2 & . \end{bmatrix} \frac{\partial}{\partial z}\begin{bmatrix} v_y^{(1)} \\ B_y^{(1)} \end{bmatrix} = \boldsymbol{0},$$

and yields a dispersion relation

$$\omega^2(x) - k_z^2 v_A^2(x) = 0$$

that describes a continuous spectrum of local Alfvén waves that are linearly polarized along y. They propagate parallel to the y,z plane at local Alfvén speeds $v_A(x)$. The frequency of the incoming wave matches that of the local Alfvén continuum at planes $x = x^*$ where the local Alfvén speed satisfies

$$v_A(x^*) = \pm\omega/k_z. \tag{8}$$

If $k_y \neq 0$ (otherwise $v_y^{(1)}$ and $B_y^{(1)}$ are **0**) and $k_z \neq 0$ (otherwise there is no field-aligned wave component), there is a coupling between the incident wave and these local Alfvén waves. If thermal pressure cannot be ignored, resonances can also occur with local slow magnetoacoustic modes [*Čadež et al.*, 1997; *De Keyser et al.*, 1999].

The energy flux in a dissipationless low beta plasma is the Poynting flux $\boldsymbol{P} = \boldsymbol{E} \times \boldsymbol{B}/\mu_0$. The equilibrium flux is zero. The first-order flux in the x direction

$$P_x^{(1)} = \frac{B^{(0)2}}{\mu_0} v_x^{(1)},$$

has a zero time average in a periodically driven system. The time-averaged second-order flux can be shown to be

$$\langle P_x^{(2)} \rangle = \frac{B^{(0)}}{\mu_0} \langle v_x^{(1)} B_z^{(1)} \rangle.$$

The energy flux carried by a monochromatic wave in a uniform medium is

$$\langle P_x^{(2)} \rangle = \frac{1}{\mu_0} \cos\phi \cos\theta \, v_A \, \langle B_{\text{peak}}^{(1)2} \rangle,$$

that is, energy density times wave velocity projected onto the x direction. We define the transmission, reflection, and absorption coefficients as the fraction of the time-averaged flux that is transmitted, reflected, or absorbed, relative to the average incident flux:

$$\begin{aligned} \alpha_t &= \frac{v_{A,\text{msph}}}{v_{A,\text{msh}}} (B_t^{(1)}/B_i^{(1)})^2, \\ \alpha_r &= (B_r^{(1)}/B_i^{(1)})^2, \\ \alpha_a &= 1 - \alpha_t - \alpha_r, \end{aligned}$$

where $B_i^{(1)}$, $B_t^{(1)}$, and $B_r^{(1)}$ represent the amplitudes of the incident, transmitted, and reflected waves.

3. Numerical Solution

We set $q^{(1)}(x, y, z, t) = \hat{q}(x, t) \exp i(k_y y + k_z z)$. With $\tilde{\boldsymbol{q}} = [b\hat{v}_x, ib\hat{v}_y, i\hat{B}_x/b, \hat{B}_y/b, \hat{B}_z/b]$, (7) becomes

$$\begin{aligned} \frac{1}{v_A}\frac{\partial \tilde{\boldsymbol{q}}}{\partial t} + \tilde{\mathcal{A}}_x \frac{\partial}{\partial x}\tilde{\boldsymbol{q}} &= -(k_y \tilde{\mathcal{A}}_y + k_z \tilde{\mathcal{A}}_z + \frac{1}{b}\frac{db}{dx}\tilde{\mathcal{S}})\tilde{\boldsymbol{q}} \\ &+ \frac{\eta}{v_A}[(\frac{1}{b}\frac{d^2 b}{dx^2} - k_y^2 - k_z^2) + \frac{2}{b}\frac{db}{dx}\frac{\partial}{\partial x} + \frac{\partial^2}{\partial x^2}]\tilde{\mathcal{C}}\tilde{\boldsymbol{q}}, \end{aligned} \tag{9}$$

where $\tilde{\mathcal{C}} = \mathcal{C}$, and

$$\tilde{\mathcal{A}}_x=\begin{bmatrix} . & . & . & . & 1 \\ . & . & . & . & . \\ . & . & . & . & . \\ . & . & . & . & . \\ 1 & . & . & . & . \end{bmatrix}, \quad \tilde{\mathcal{A}}_y=\begin{bmatrix} . & . & . & . & . \\ . & . & . & . & -1 \\ . & . & . & . & . \\ . & . & . & . & . \\ . & 1 & . & . & . \end{bmatrix},$$

$$\tilde{\mathcal{A}}_z=\begin{bmatrix} . & . & -1 & . & . \\ . & . & . & 1 & . \\ 1 & . & . & . & . \\ . & -1 & . & . & . \\ . & . & . & . & . \end{bmatrix}, \quad \tilde{\mathcal{S}} = \begin{bmatrix} . & . & . & . & 1 \\ . & . & . & . & . \\ . & . & . & . & . \\ . & . & . & . & . \\ -1 & . & . & . & . \end{bmatrix}.$$

The particular scaling of the state vector serves to keep all

coefficients real ($\hat{v}_y$ and $\hat{B}_x$ are phase-shifted with respect to the other components) and to keep $\tilde{\mathcal{A}}_x$ constant.

3.1. Spatial Discretization

Every spatial discretization introduces an equivalent "numerical diffusion" (discontinuities can be represented only with a finite spatial resolution). This numerical diffusion is also present when numerically solving the dissipationless equations. In our simulations we always use a physical diffusion $\eta > 0$. We make sure that it exceeds the numerical diffusion by taking the spatial discretization accurate enough so as to obtain mesh-independent results.

We employ a finite volume spatial discretization. The domain $[x_{\mathrm{msph}}, x_{\mathrm{msh}}]$ is discretized using an equidistant mesh with mesh spacing h. Equations (9), integrated over a mesh cell Ω_i centered around x_i, result in

$$\frac{1}{v_{A,i}}\frac{\partial \tilde{q}_i}{\partial t} + \frac{1}{h}[\tilde{f}_{x,i+\frac{1}{2}} - \tilde{f}_{x,i-\frac{1}{2}}] = \tilde{g}_i,$$

with cell-averaged state vector

$$\tilde{q}_i = \int_{\Omega_i} \tilde{q}(x,y,z)\mathrm{d}\Omega/h,$$

and similarly cell-averaged right hand side $\tilde{g}_i$. The numerical flux $\tilde{f}_{x,i\pm\frac{1}{2}}$ approximates the flux from right to left at the interface between Ω_i and $\Omega_{i\pm1}$. Given states $\tilde{q}_L$ and $\tilde{q}_R$ on either side of the interface between Ω_i and Ω_{i+1}, the numerical flux is obtained by a Roe-type approximate Riemann solver:

$$\tilde{f}_{x,i+\frac{1}{2}} = \frac{1}{2}[\tilde{f}_x(\tilde{q}_L) + \tilde{f}_x(\tilde{q}_R) - \tilde{d}_x(\tilde{q}_L, \tilde{q}_R)]$$

with $\tilde{f}_x(\tilde{q}) = \tilde{\mathcal{A}}_x\tilde{q}$ and

$$\tilde{d}_x = \sum_\alpha |\tilde{\lambda}_x^\alpha|\tilde{r}_x^\alpha \tilde{l}_x^\alpha(\tilde{q}_R - \tilde{q}_L) = \begin{bmatrix} \tilde{v}_{xR} - \tilde{v}_{xL} \\ \cdot \\ \cdot \\ \cdot \\ \tilde{B}_{zR} - \tilde{B}_{zL} \end{bmatrix},$$

where $\tilde{\lambda}_x^\alpha$, $\tilde{r}_x^\alpha$, and $\tilde{l}_x^\alpha$ are the eigenvalues and the right and left eigenvectors of $\tilde{\mathcal{A}}_x$ (which are constant due to the particular scaling). The accuracy of the numerical flux depends on the order of accuracy with which $\tilde{q}_L$ and $\tilde{q}_R$ are approximated. As the system is second-order in space, the spatial discretization must be (at least) second-order accurate. For the interface between Ω_i and Ω_{i+1} we use the approximations (for each state variable)

$$\tilde{q}_L = \tilde{q}_i + \frac{h}{2}\phi\left(\frac{\nabla_+\tilde{q}_{i+1}}{\nabla_-\tilde{q}_i}\right)\nabla_-\tilde{q}_i, \quad (10)$$

$$\tilde{q}_R = \tilde{q}_{i+1} - \frac{h}{2}\phi\left(\frac{\nabla_-\tilde{q}_i}{\nabla_+\tilde{q}_{i+1}}\right)\nabla_+\tilde{q}_{i+1}, \quad (11)$$

where $\nabla_+\tilde{q}_{i+1} = (\tilde{q}_{i+2} - \tilde{q}_{i+1})/h$ and $\nabla_-\tilde{q}_{i+1} = (\tilde{q}_{i+1} - \tilde{q}_i)/h$. Factor ϕ is a so-called flux limiter. It is not needed when the solution is smooth; $\tilde{q}_L$ is then obtained from a piecewise linear extrapolation of $\tilde{q}_{i-1}$ and $\tilde{q}_i$, and $\tilde{q}_R$ from $\tilde{q}_{i+2}$ and $\tilde{q}_{i+1}$. The scheme then is second-order accurate in space. We are dealing, however, with solutions that are not continuous or not continuously differentiable because of the discontinuous boundary conditions. (If system (9) would have been nonlinear, discontinuous solutions could arise even for continuous boundary conditions.) The purpose of the flux limiter is to avoid the adverse effects of unwarranted extrapolation when discontinuities are present. Consider formula (10). If $\nabla_+\tilde{q}_{i+1}$ and $\nabla_-\tilde{q}_i$ have opposite sign, possibly indicating a discontinuity between x_i and x_{i+1}, full limiting is applied ($\phi = 0$). If both gradients have the same sign with $\nabla_+\tilde{q}_{i+1} \ll \nabla_-\tilde{q}_i$, there might be a discontinuity too. If the gradient does not change much ($\nabla_+\tilde{q}_{i+1} \approx \nabla_-\tilde{q}_i$), the solution is continuous and no limiting is needed ($\phi(1) = 1$). If $\nabla_+\tilde{q}_{i+1} \gg \nabla_-\tilde{q}_i$ the value of ϕ is not critical as it is multiplied with a small quantity. We prefer the minmod limiter ($\phi(s) = 0$ for $s \le 0$, $\phi(s) = s$ for $0 < s \le 1$, and $\phi(s) = 1$ for $s > 1$). The choice of limiter influences the solution on a subgrid resolution scale. It affects the precise form of the numerical diffusion of the discrete scheme: It adds diffusion near discontinuities in the solution so that the spatial accuracy is of order 1 there, while it remains effectively second-order elsewhere. The mesh parameter h obviously must be fine enough to resolve the waves, that is, $hk \ll 1$.

3.2. Time Discretization

We use explicit time integration methods to solve system (9). Stability constrains the maximum time step Δt to be of the order of the Courant-Friedrichs-Lewy limit $\Delta t_{\mathrm{CFL}} = h/v_A$, that is, the mesh spacing divided by the fastest wave speed. The dimensionless time step $\tau_{\mathrm{CFL}} = \Delta t/\Delta t_{\mathrm{CFL}}$ therefore is of order unity. Since $\omega\Delta t = \omega\tau_{\mathrm{CFL}}\Delta t_{\mathrm{CFL}} = \tau_{\mathrm{CFL}}h\omega/v_A = \tau_{\mathrm{CFL}}hk \ll 1$, the timescale of the boundary conditions is resolved if the spatial resolution is sufficient too.

System (9) is first order in time. First-order time-accurate Forward Euler integration (FE) can therefore be used. The solution $\tilde{q}_{l+1}$ at time step $l+1$ is computed from that at time l by

$$\tilde{q}_{l+1} = \tilde{q}_l + \Delta t_l\tilde{\mathcal{R}}\tilde{q}_l,$$

where the residual at time step l is given by

$$\tilde{\mathcal{R}}\tilde{q}_{l,i} = v_{A,i}[\tilde{g}_{i,l} - \frac{1}{h}(\tilde{f}_{x,i+\frac{1}{2},l} - \tilde{f}_{x,i-\frac{1}{2},l})].$$

It is straightforward to show that the relative discretization error for FE combined with the second-order in space Roe-type flux without limiter satisfies:

$$\epsilon_l \sim l\frac{\tau_{\mathrm{CFL}}^2}{2}(hk)^2,$$

as long as $\epsilon_l < 1$. This means that the total discretization error grows linearly with the number of time steps as long as it is small (when ϵ_l becomes larger, the error grows exponentially). The numerical solution becomes worthless when $\epsilon_l \sim 1$, that is, after

$$l_{\max} \sim \frac{2}{\tau_{\mathrm{CFL}}^2 (hk)^2}$$

time steps. This corresponds to a simulation time

$$t_{\mathrm{sim}} = l_{\max}\Delta t \sim \frac{2}{\tau_{\mathrm{CFL}}(hk)(kv_A)} = \frac{T}{\tau_{\mathrm{CFL}}\pi hk},$$

where T is the wave period. The number of wave periods that can be simulated with FE with a given spatial resolution $(hk)_{\mathrm{FE}}$ therefore is

$$\nu_{\mathrm{FE}} \propto (hk)_{\mathrm{FE}}^{-1}.$$

The computational complexity of the time-dependent simulation with FE is

$$C_{\mathrm{FE}} \propto l_{\max}(hk)_{\mathrm{FE}}^{-1} \propto (hk)_{\mathrm{FE}}^{-3} \propto \nu_{\mathrm{FE}}^3,$$

as every time step involves a solution update in each mesh point (there are of the order of $(hk)^{-1}$ mesh points).

We also use multistage Runge-Kutta integrators, in particular the two-stage RK2(1/2,1) scheme, also known as Heun's method, which is second order accurate in time:

$$\begin{aligned} \tilde{q}_{l+\frac{1}{2}} &= \tilde{q}_l + \frac{1}{2}\Delta t_l \tilde{\mathcal{R}}\tilde{q}_l, \\ \tilde{q}_{l+1} &= \tilde{q}_l + \Delta t_l \tilde{\mathcal{R}}\tilde{q}_{l+\frac{1}{2}}. \end{aligned}$$

This scheme, combined with second-order spatial accuracy, Roe-type flux, and without limiter, has a relative discretization error

$$\epsilon_l \sim lK(hk)^3$$

with K a constant of order unity. It allows

$$l_{\max} \sim \frac{1}{K(hk)^3}$$

time steps, equivalent to a simulation time

$$t_{\mathrm{sim}} = l_{\max}\Delta t \sim \frac{\tau_{\mathrm{CFL}}}{2\pi K}\frac{T}{(hk)^2},$$

that is,

$$\nu_{\mathrm{Heun}} \propto (hk)_{\mathrm{Heun}}^{-2}.$$

Each time step now requires two updates in each mesh point. The computational complexity of the simulation is

$$C_{\mathrm{Heun}} \propto (hk)_{\mathrm{Heun}}^{-4} \propto \nu_{\mathrm{Heun}}^2.$$

Comparing both methods for a given ν, which is the physically relevant parameter, we see that $C_{\mathrm{Heun}} \propto \nu^2 < C_{\mathrm{FE}} \propto \nu^3$, at least when ν is large enough so that the proportionality constants do not matter anymore. With Heun's method the discretization error grows slower, such that less mesh points and less time steps are needed.

3.3. Initial Condition and Boundary Conditions

We start from an initially unperturbed system, that is, $\hat{q}(x, t_0 = 0) \equiv 0$. The boundary conditions at the left end of the domain specify that there is no wave originating in the magnetosphere that enters the simulation domain. The boundary conditions on the right end describe a monochromatic wave that enters the simulation domain at time $t_0 \geq 0$. The boundary conditions only specify incoming waves: The Roe-type flux difference splitter automatically ensures that outgoing waves simply leave the domain.

This combination of initial and boundary conditions imply that the driver is a periodic wave multiplied by a step function (0 if $t < t_0$, 1 if $t \geq t_0$). It is this step function that prohibits the use of a single Fourier mode approach; the step function is also responsible for the occurrence of transient phenomena. The driver is not strictly monochromatic as the step function introduces additional Fourier components; it is monochromatic, however, in any time window that does not include t_0.

In a low beta plasma the incident wave can be either an Alfvén or a fast wave. The conditions for mode resonance at the plasma inhomogeneity can only be satisfied for an incident fast wave. We specify the incidence direction by wave vector azimuth ϕ (angle between $[k_x, k_y, 0]$ and the x axis, between 180° and 270°) and elevation θ (angle between $\boldsymbol{k}$ and the x,y plane), which imply tangential wave numbers $k_y = \omega\cos\theta\sin\phi/v_A$ and $k_z = \omega\sin\theta/v_A$. The boundary condition then is

$$\begin{aligned} \hat{v}_x(x_{\mathrm{msh}}, t) &= -v_A\frac{\cos\phi}{\cos\theta}\frac{B_{\mathrm{ref}}}{B^{(0)}}\sin(\omega t), \\ i\hat{v}_y(x_{\mathrm{msh}}, t) &= v_A\frac{\sin\phi}{\cos\theta}\frac{B_{\mathrm{ref}}}{B^{(0)}}\cos(\omega t), \\ i\hat{B}_x(x_{\mathrm{msh}}, t) &= -\tan\theta\cos\phi B_{\mathrm{ref}}\cos(\omega t), \\ \hat{B}_y(x_{\mathrm{msh}}, t) &= \tan\theta\sin\phi B_{\mathrm{ref}}\sin(\omega t), \\ \hat{B}_z(x_{\mathrm{msh}}, t) &= -B_{\mathrm{ref}}\sin(\omega t), \end{aligned}$$

where B_{ref} is an arbitrary scaling constant. For a given medium and a given frequency, the incident wave's wave number is fixed by the dispersion relation for fast waves. Both $i\hat{v}_y$ and $i\hat{B}_x$ are discontinuous at $t_0 = 0$; the other state variables are not continuously differentiable there.

4. Development of a Resonant Sheet

Figure 2 illustrates the time-dependent behavior of a resonant sheet. We consider a wave with frequency $f = 0.5$ Hz and incidence direction $\phi = 135°$, $\theta = 45°$. The magnetic diffusivity is $\eta = 5 \times 10^6$ m^2 s^{-1}. This corresponds to a magnetic Reynolds number $Rm = v_A^2/f\eta \sim 10^5$ (the precise value depends on which v_A is used). We used Heun's method with $\tau_{\mathrm{CFL}} = 0.5$, second-order spatial accuracy, minmod limiter, and 2000 discretization points, to simulate the propagation of the incident wave in the region $[-3000, +3000]$ km during 80 s (40 wave periods). The simulated magnetic field perturbations are plotted as functions of space and time (at y=z=0). It takes about 12 s before the incident wave reaches the transition layer, where it is partially absorbed and partially reflected (there is no transmission in this particular case). The reflected wave moves with

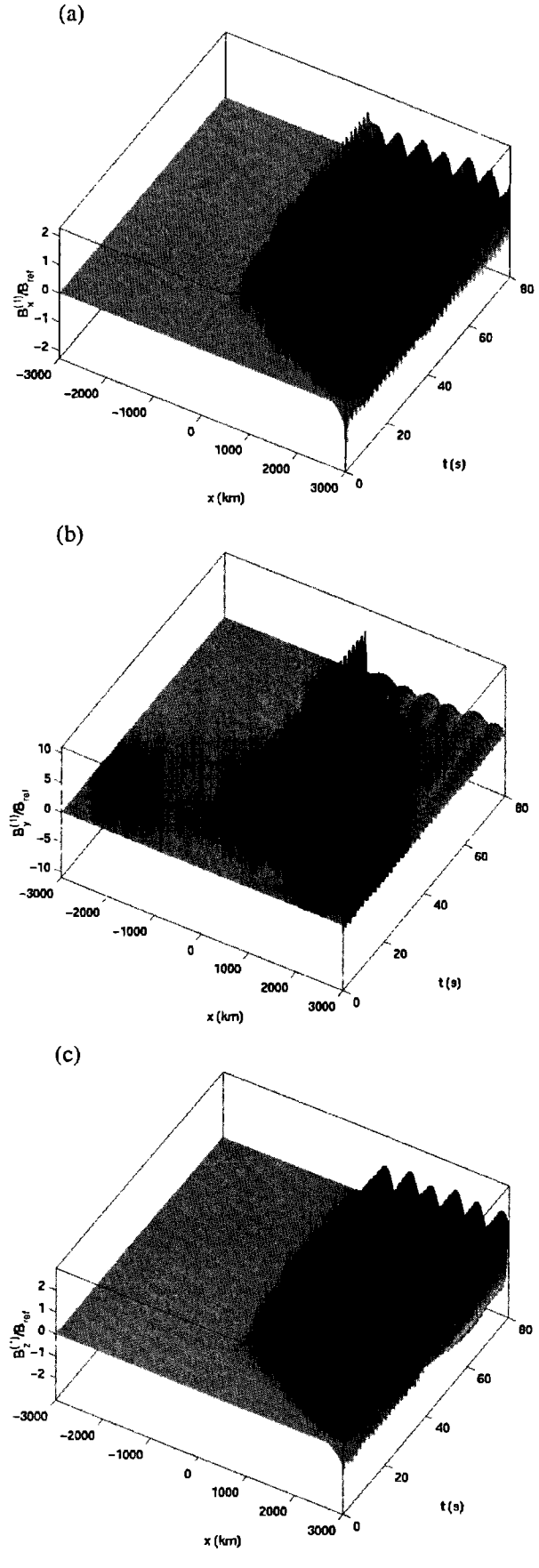

the same speed as the incident wave but in the opposite direction (wave vector $[-k_x, k_y, k_z]$). As soon as the incident wave reaches the transition layer, the perturbation amplitude starts to grow exponentially as a resonant sheet begins to form, which can be seen in Figures 2a and 2b. The resonance does not show up in the B_z perturbation (Figure 2c), as it is a transverse Alfvén wave that travels along the magnetic field lines and thus does not have a B_z component. The development of the resonance is traced in Figure 3a, which plots the maximum magnetic field perturbation $\max_{x,y,z} B^{(1)}$ in the simulation domain as a function of time; after an initial transitory period, this is the wave amplitude in the resonant sheet. After about 40 s the growth ceases to be exponential: The wave amplitude in the narrow resonant layer is so large that the second order spatial derivatives and hence the diffusive flux can no longer be neglected. After 30 wave periods (~60 s) the resonance saturates at ~5 times the incident wave amplitude. Since $\nabla \cdot \boldsymbol{B}^{(1)} = 0$, and because the variations in x, y, and z occur over length scales δ (thickness of the resonant sheet), $\lambda_y = 2\pi/k_y$, and $\lambda_z = 2\pi/k_z$, respectively, and also because for the B_z component of the local Alfvén waves is zero, the resonant amplitudes at saturation are related by $B^{(1)}_{x,\mathrm{sat}} \sim \delta_{\mathrm{sat}} k_y B^{(1)}_{y,\mathrm{sat}}$; as will be discussed later on, δ_{sat} decreases when $\eta \to 0$ so that $B^{(1)}_{x,\mathrm{sat}} \ll B^{(1)}_{y,\mathrm{sat}}$. Figure 3b plots the maximum magnetic field perturbation $\max_{t,y=0,z=0} B^{(1)}$ during one wave period as a function of position, after the saturation regime is established. The resonant layer is about 50 km thick (full width at half maximum 20 km), which corresponds to 16 mesh points, so that it is well resolved by the simulation (implying that numerical diffusion is dwarfed by physical diffusion, that is, the solution shown here is essentially mesh independent; we have verified this by repeating the simulation with the double number of mesh points). Once the system has reached a quasi-steady situation, a fixed fraction of the incident wave power is absorbed and dissipated around the resonant layer, while the remainder is reflected and transmitted (in this particular example there is no transmission). Constructive interference between the incident left-going wave and the reflected right-going wave, both with the same frequency, leads to

Figure 2. Magnetic field perturbation for a wave with frequency $f = 0.5$ Hz and incidence angles $\phi = 135°$ and $\theta = 45°$ traveling through a medium with magnetic diffusivity 5×10^6 m^2 s^{-1}. The x axis goes from -3000 to +3000 km (the transition has half thickness 300 km and is centered around $x = 0$). The time axis covers a period of 80 s or 40 wave periods. (a) Magnetic perturbation x component $B_x^{(1)}(x,0,0,t)/B_{\mathrm{ref}}$ featuring a small peak in the mode conversion layer. (b) Magnetic perturbation y component $B_y^{(1)}(x,0,0,t)/B_{\mathrm{ref}}$ showing a strong peak in the mode conversion layer. (c) Magnetic perturbation z component $B_z^{(1)}(x,0,0,t)/B_{\mathrm{ref}}$ showing no sign of the resonance as the local Alfvén wave has no field-aligned component.

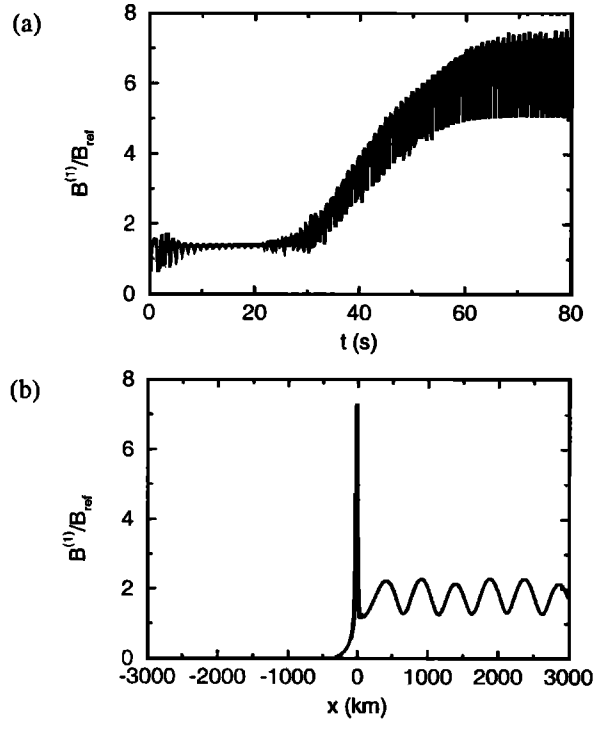

Figure 3. Same problem as in Figure 2. (a) Maximum magnitude of the magnetic perturbation over space as a function of time $\max_{x,y,z} B^{(1)}(t)/B_{\text{ref}}$ showing the starting period during which the wave propagates toward the transition, the initial exponential growth of the resonant sheet amplitude, and its saturation. (b) Maximum magnitude of the magnetic perturbation over a wave period as a function of distance from the transition $\max_t B^{(1)}(x,0,0)/B_{\text{ref}}$ in the saturated regime.

a peak amplitude equaling the sum of the incident and reflected wave amplitudes. The peak amplitude is about 1.85 times the incident wave amplitude, implying that the reflected wave amplitude is 85% of the incident one. About 72% of the incident wave power is therefore reflected; 28% is dissipated in the resonant sheet.

The time-dependent saturation process found here differs from that found in other systems. The transient behavior of cylindrical flux tubes, periodically driven at frequencies that belong to the local mode continuum, is affected by the presence of quasi-modes with a frequency close to the driver frequency. These quasi-modes may be excited in the initial stages of the development of the resonance, as the step function associated with the start of the driver implies a broad frequency content, and they may cause transient wave beating phenomena; a significantly different transient behavior is found when one drives the quasi-modes (or other discrete eigenmodes of the system) directly [*Poedts et al.*, 1990; *Poedts and Kerner*, 1992]. Another interesting situation occurs when the field lines have a finite length. Such a system also has discrete eigenmodes (field line resonances); the transient behavior of driven field line resonances is different from what is obtained here [*Mann et al.*, 1995].

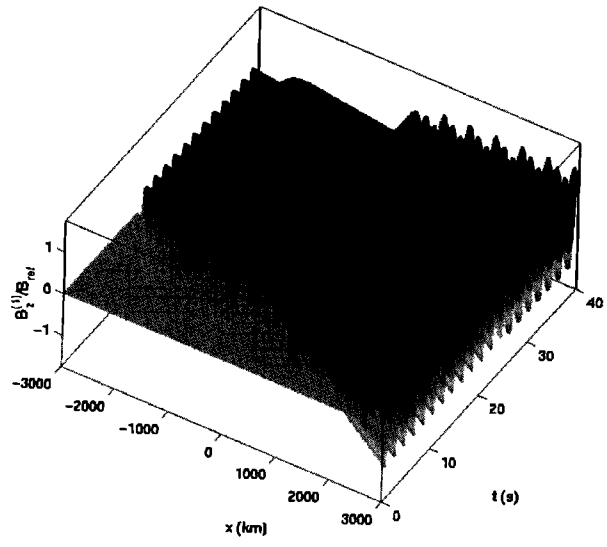

Figure 4. Magnetic field perturbation for a wave with frequency $f = 0.5$ Hz at normal incidence ($\phi = 180°$ and $\theta = 0°$) traveling through a medium with magnetic diffusivity 5×10^6 m^2 s^{-1}. The x axis goes from -3000 to +3000 km (the transition has half thickness 300 km and is centered around $x = 0$). The time axis covers a period of 40 s or 20 wave periods. $B_z^{(1)}$ is nonzero, while $B_x^{(1)} = B_y^{(1)} \equiv 0$. There is no resonance, but the wave is partly reflected, partly transmitted.

Another example is the normal incidence case ($\phi = 180°$, $\theta = 0°$, implying $k_y = k_z = 0$) shown in Figures 4 and 5 (frequency $f = 0.5$ Hz) in which only the z component of magnetic field perturbation is nonzero. There can be no resonant amplification in this case, only partial transmission and reflection. The peak magnetic field amplitude in the magnetosheath is about 1.15 times the amplitude of the

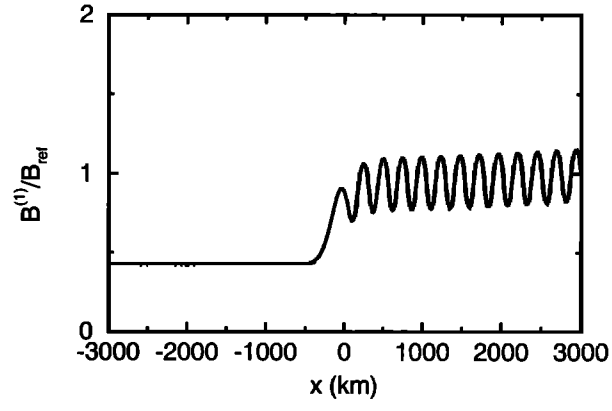

Figure 5. Same problem as in Figure 4. The plot shows the maximum magnitude of the magnetic perturbation over a wave period as a function of distance from the transition $\max_t B^{(1)}(x,0,0)/B_{\text{ref}}$ at the end of the simulation.

incident wave: Only 2.25% of the incident wave power is reflected, the remainder is transmitted. In the absence of absorption, energy conservation dictates the transmitted wave amplitude:

$$B_{\rm t}^{(1)} = \sqrt{\frac{v_{A,\rm msh}}{v_{A,\rm msph}}(B_{\rm i}^{(1)2} - B_{\rm r}^{(1)2})}$$

or $0.47B_{\rm ref}$, which is almost what we find in the simulation. The nonzero magnetic diffusion leads to some energy dissipation as the incident wave travels toward the transition, resulting in a slightly decreasing wave amplitude in the magnetosheath (as can be seen in Figure 5). In this way the principle of conservation of energy provides a numerical check on the solution.

We have also performed simulations (not shown) for incidence directions for which there is no transmission and no absorption (e.g., $\phi = 180°$, $\theta = 45°$). In that case, 100% of the energy flux is reflected and a standing wave pattern is established in the magnetosheath.

5. Effect of Diffusion

Magnetic diffusion plays a crucial role in establishing the saturated Alfvén resonant sheet. The dependence of the sheet's thickness $\delta_{\rm sat}$ on the diffusion coefficient and on the frequency is well established [*Goossens and Ruderman*, 1995]; for the static low beta case it can be expressed as

$$\delta_{\rm sat}(\eta,\omega) = \left(\frac{\rho^{(0)}\eta}{\omega \sin^2\theta |d\ln\rho^{(0)}/dx|}\right)^{1/3} \propto \eta^{1/3}.$$

As expected, the thickness $\delta_{\rm sat}$ decreases with the dissipation level, since infinitely narrow resonances are associated with the dissipationless case. The dependency on ω is less obvious, since a frequency change shifts the resonant position and affects $d\ln\rho^{(0)}/dx$; one expects $\delta_{\rm sat} \propto \omega^{-1/3}$ for frequencies that correspond to a resonance near the center of the transition layer, where the density gradient is essentially constant.

Is is also well established that the resonantly absorbed energy flux is essentially independent of η as long as it is small [*Southwood*, 1974]. At saturation the Ohmic dissipation in the layer per unit time must equal the net wave energy flux normal to the slab (which can be expressed in terms of the absorption coefficient and the incident wave amplitudes as specified by the boundary conditions):

$$\alpha_{\rm a}\frac{B^{(0)}}{\mu_0}v_{x,\rm inc}^{(1)}B_{z,\rm inc}^{(1)} = \eta\mu_0 j_{\rm sat}^2\delta_{\rm sat}.$$

With the current density $j_{\rm sat} = B_{\rm sat}/\mu_0\delta_{\rm sat}$ one finds the magnetic field amplitude in the resonance at saturation:

$$B_{\rm sat}^2(\eta,\omega) = \alpha_{\rm a}v_A\frac{\cos\phi}{\cos\theta}\frac{\delta_{\rm sat}(\eta,\omega)}{\eta}B_{\rm ref}^2 \propto \delta_{\rm sat}(\eta,\omega)/\eta.$$

Therefore $B_{\rm sat} \propto \eta^{-1/3}$: With smaller dissipation coefficient, larger second-order derivates are needed for the diffusive flux to be of the same order of magnitude as the convective fluxes, implying a larger resonant amplitude. This is consistent with the infinite amplitudes that are obtained in the dissipationless case. For resonances near the center of the layer, the ω dependence of the saturation amplitude is $B_{\rm sat} \propto {\delta_{\rm sat}}^{1/2} \propto \omega^{-1/6}$: It increases when frequency or diffusion coefficient become smaller. At smaller frequencies, that is, longer periods, more energy can be fed into the resonant layer by the wave during one half cycle, causing the peak amplitude to increase.

The saturation time $T_{\rm sat}$ can be estimated as follows. The incident wave supplies energy to the layer, which is partly stored in the growing local waves, and partly dissipated as Ohmic heat. Therefore

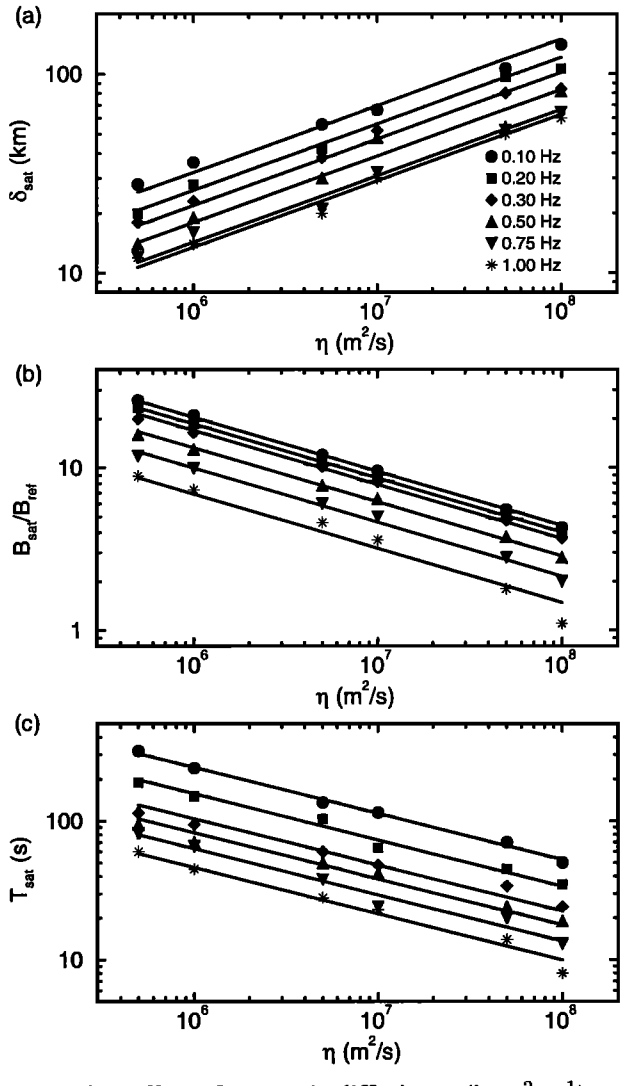

Figure 6. Effect of magnetic diffusion η (in $\rm m^2\,s^{-1}$) and frequency f (in Hertz) on (a) the resonant sheet thickness $\delta_{\rm sat}$ (in kilometers); the solid lines are least squares fits of power law scaling with exponent 1/3; (b) the peak magnetic field perturbation amplitude $B_{\rm sat}/B_{\rm ref}$ in the resonant sheet in the saturated regime; the solid lines are least squares power law fits with exponent $-1/3$; (c) the time $T_{\rm sat}$ (in seconds) needed to reach saturation; the solid lines again fit power law behavior with exponent $-1/3$.

$$\left(\frac{\rho^{(0)}v_{\rm sat}^2}{2}+\frac{B_{\rm sat}^2}{2\mu_0}\right)\delta_{\rm sat} \lesssim \int_{t_0}^{t_0+T_{\rm sat}} \alpha_{\rm a}\frac{B^{(0)}}{\mu_0}\, v_{x,\rm inc}^{(1)} B_{z,\rm inc}^{(1)}\, dt,$$

where the left-hand side represents the energy in the resonant waves, and the right-hand side represents the energy supplied to the layer; the inequality comes from ignoring the dissipation during the growth phase. Consequently,

$$T_{\rm sat}(\eta,\omega) \lesssim \frac{\delta_{\rm sat}(\eta,\omega)}{\alpha_{\rm a} v_A}\left(\frac{\rho^{(0)}v_{\rm sat}^2}{2}+\frac{B_{\rm sat}^2}{2\mu_0}\right)/\left(\frac{B_{\rm ref}^2}{2\mu_0}\right),$$

from which we find a scaling $T_{\rm sat} \propto \delta_{\rm sat} B_{\rm sat}^{(1)2} \propto \eta^{-1/3}$. A rigorous derivation is given by *Kappraff and Tataronis* [1977]. The fact that $T_{\rm sat}$ becomes larger when the diffusion becomes smaller is consistent with the absence of saturation for vanishing diffusion.

Figure 6 illustrates the scaling laws of $\delta_{\rm sat}$, $B_{\rm sat}/B_{\rm ref}$, and $T_{\rm sat}$ with η for different frequencies. Superimposed on the values obtained from the simulations, we plot the least squares power law fits with the known exponents; the data follow these exponential laws fairly well. These plots constitute a validation of the numerical code. They confirm that the accuracy of the simulations was sufficient to resolve the resonant sheet (that is, that the numerical dissipation remains well below the physical dissipation), something that we have also checked by simply counting the number of mesh points that resolve the resonant layer.

6. Effect of Incidence Angle

The fast wave dispersion relations in the magnetosheath and in the magnetosphere are

$$\begin{aligned} k_{x,\rm msh}^2 + k_y^2 + k_z^2 &= \omega^2/v_{A,\rm msh}^2, \\ k_{x,\rm msph}^2 + k_y^2 + k_z^2 &= \omega^2/v_{A,\rm msph}^2. \end{aligned}$$

As the incident wave is a propagating one, $k_{x,\rm msh}^2 > 0$. Propagation of the wave in the magnetosphere occurs when

$$k_{x,\rm msph}^2 = \frac{\omega^2}{v_{A,\rm msph}^2}\left[1-\frac{v_{A,\rm msph}^2}{v_{A,\rm msh}^2}(\cos^2\theta\sin^2\phi+\sin^2\theta)\right] > 0,$$

or

$$\frac{\rho_{\rm msph}}{\rho_{\rm msh}} > \cos^2\theta\sin^2\phi+\sin^2\theta,$$

which depends only on the incidence direction, but not on the frequency. For the equilibrium considered here, transmission occurs only for incident waves propagating less than $\sim 13°$ away from the normal.

We have systematically examined the effect of the incidence direction on the characteristics of the resonant layer and summarize the results in Figure 7. The saturation time $T_{\rm sat}$ and the amplitude $B_{\rm sat}$ are large for grazing incidence angles. In Figure 8 we plot the transmission, reflection, and absorption coefficients. It is physically obvious that no mode conversion occurs when $\theta = 0°$: When $k_z = 0$ the Alfvén mode disappears from the dispersion relation, so that it cannot be excited. Also, mode conversion does not occur when $\phi = 0°$: As resonant waves are linearly polarized with only

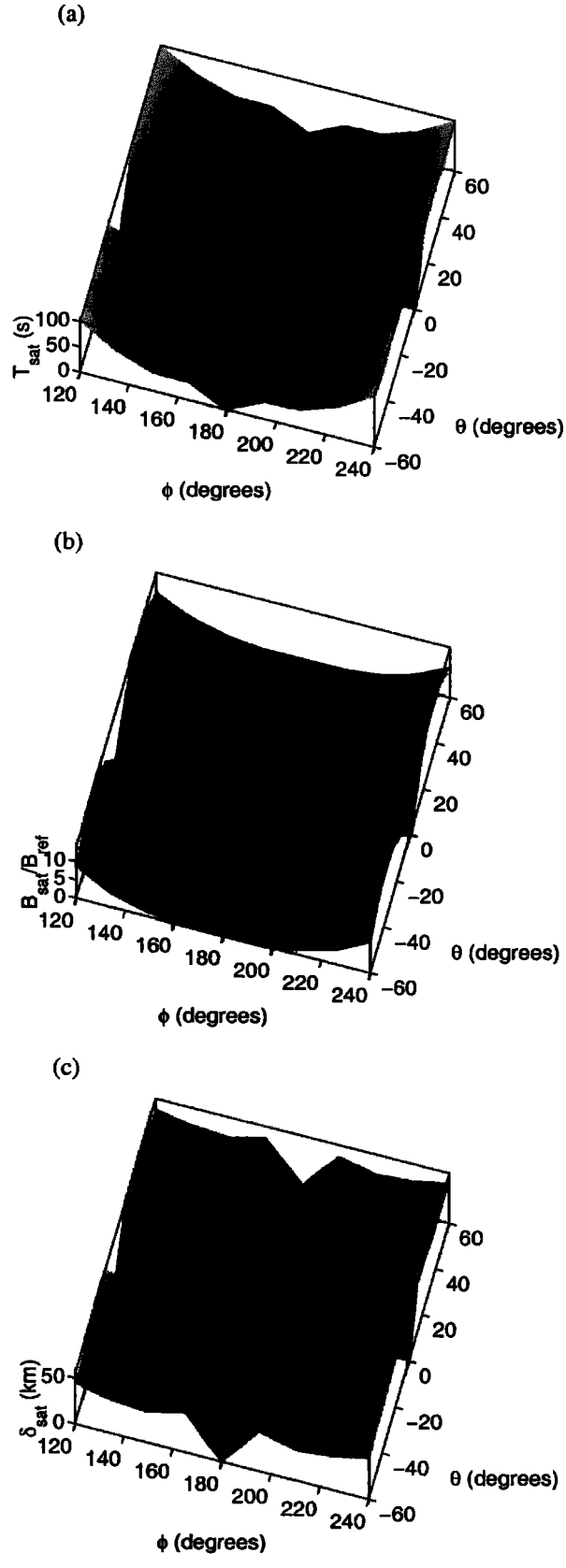

Figure 7. Effect of incidence angles ϕ and θ on (a) the time $T_{\rm sat}$ needed to reach saturation, in seconds, (b) the peak magnetic field perturbation amplitude $B_{\rm sat}$ in the resonant sheet in the saturated regime, relative to the incident wave amplitude, and (c) the resonant sheet half width $\delta_{\rm sat}$, in kilometers.

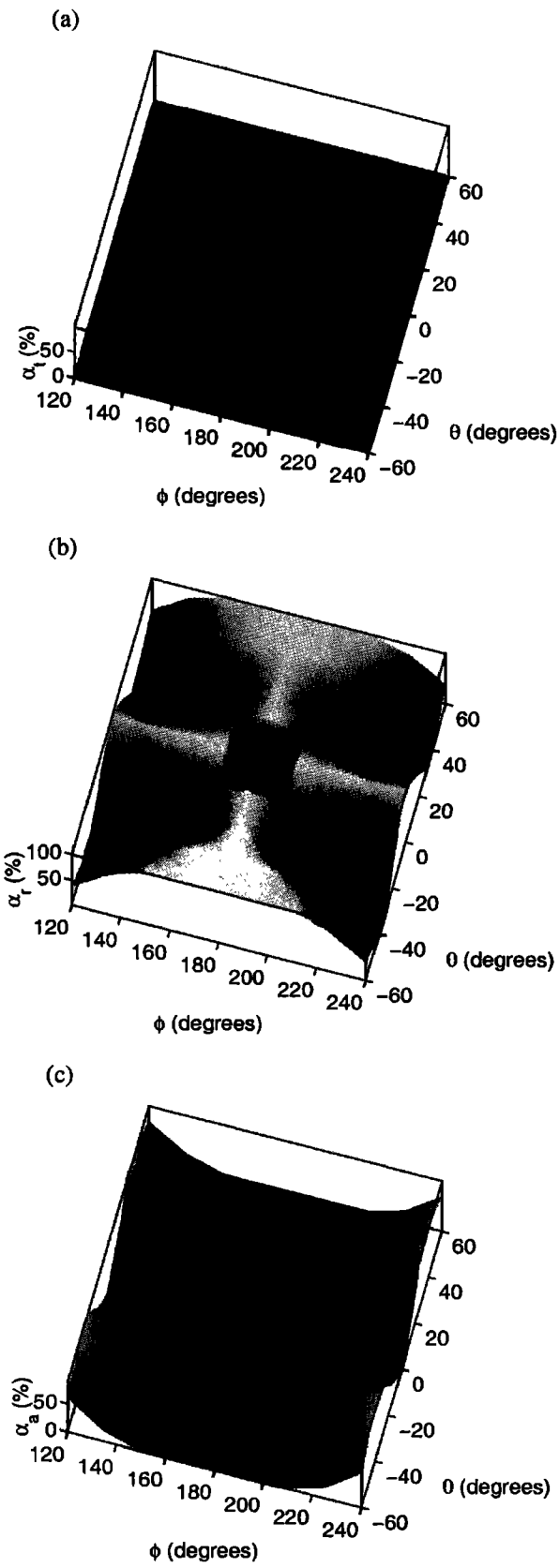

Figure 8. Effect of incidence angles ϕ and θ on (a) the transmission coefficient α_t, (b) the reflection coefficient α_r, and (c) the absorption coefficient α_a.

a $v_y^{(1)}$ component, they cannot be excited when $k_y = 0$. This absence of resonance shows up as a cross-shaped minimum in the absorption coefficient and a corresponding maximum in the reflection coefficient, except near normal incidence where transmission plays a role.

7. Conclusions

In this paper we have determined the transient response of the magnetopause to an incident monochromatic wave. We have identified the circumstances required for mode conversion and for the formation of a resonant layer in which growing perturbation amplitudes saturate after some time due to diffusive effects.

Magnetosheath waves are never really monochromatic, but they have a broadband nature [*Anderson et al.*, 1982]. This broadband nature has two consequences: (1) Due to the continuous frequency spectrum, each place in the transition layer can be considered a resonant layer corresponding to a frequency present in the incident broadband waves. (2) As the wave power distribution over frequency changes with time, no single frequency component is driving the corresponding resonant layer long enough as to reach saturation. The net result is that the wave amplitude will be enhanced everywhere in the layer, as confirmed by observations of waves near the magnetopause [*LaBelle and Treumann*, 1988; *Rezeau et al.*, 1989; *Engebretson et al.*, 1991; *Rezeau et al.*, 1993; *Song et al.*, 1993]. A similar result was already obtained with a different approach by *De Keyser* [2000]. This is in contrast to systems with discrete eigenmodes: There a broadband driver will preferentially excite the eigenmodes of the system and thus produce enhanced amplitudes resonant points corresponding to the eigenfrequencies [*Wright and Rickard*, 1995].

The merit of this paper lies in the study of resonant mode conversion as a fundamental mechanism that determines hydromagnetic wave propagation and amplification at the magnetopause. The enhanced magnetic field fluctuation levels are important in view of the transport of mass across the magnetopause. It is still not clear at present which mass transport mechanisms operate at the magnetopause and what their relative importance is [*Sibeck et al.*, 1999]. Within the framework of ideal MHD, no net mass transport across the layer is possible. However, when kinetic effects are taken into account, the enhanced fluctuation levels play an important role. An enhancement by an order of magnitude, as we found in our simulations, strongly promotes scattering by wave-particle interactions, for instance, and contributes to diffusive transport of mass across the magnetospheric boundary [*Treumann et al.*, 1995].

The low beta linear MHD analysis considers only frequencies below the proton gyrofrequency. The actually observed fluctuation spectra extend beyond the proton gyrofrequency, so that the inclusion of kinetic effects becomes inevitable [*Lacombe et al.*, 1995; *Johnson and Cheng*, 1997]. The observed fluctuation amplitudes also do not justify a linear treatment, and a nonlinear description of resonant absorption

should be used [*Ruderman et al.*, 1997]. Another limitation of the present model is the absence of any ionospheric coupling.

Acknowledgments. The authors thank S. Poedts and E. Rigo for providing some of the referenced material. This work was supported by PRODEX in the framework of ESA's Ulysses and Cluster II missions. The support of the Belgian Federal Office for Scientific, Technical and Cultural Affairs is acknowledged.

Michel Blanc thanks Marcel Goossens and Rudolf Treumann for their assistance in evaluating this paper.

References

Anderson, R. R., C. C. Harvey, M. M. Hoppe, B. T. Tsurutani, T. E. Eastman, and J. Etcheto, Plasma waves near the magnetopause, *J. Geophys. Res., 87*, 2087–2107, 1982.

Belmont, G., F. Reberac, and L. Rezeau, Resonant amplification of magnetosheath MHD fluctuations at the magnetopause, *Geophys. Res. Lett., 22*, 295–298, 1995.

Berchem, J., and C. T. Russell, The thickness of the magnetopause current layer: ISEE 1 and 2 observations, *J. Geophys. Res., 87*, 2108–2114, 1982.

Čadež, V. M., and J. L. Ballester, Resonant absorption of MHD surface waves in an arcade with a continuous boundary, *Astron. Astrophys., 305*, 977–983, 1996.

Čadež, V. M., Á. Csík, R. Erdélyi, and M. Goossens, Absorption of magnetosonic waves in presence of resonant slow waves in the solar atmosphere, *Astron. Astrophys., 326*, 1241–1251, 1997.

De Keyser, J., Linear magnetohydrodynamic response of the magnetopause to magnetosheath fluctuations, *J. Geophys. Res., 105*, 23,167–23,177, 2000.

De Keyser, J., M. Roth, F. Reberac, L. Rezeau, and G. Belmont, Resonant amplification of MHD waves in realistic subsolar magnetopause configurations, *J. Geophys. Res., 104*, 2399–2409, 1999.

Engebretson, M. J., N. Lin, W. Baumjohann, H. Lühr, B. J. Anderson, L. J. Zanetti, T. A. Potemra, R. L. McPherron, and M. G. Kivelson, A comparison of ULF fluctuations in the solar wind, magnetosheath, and dayside magnetosphere, 1, Magnetosheath morphology, *J. Geophys. Res., 96*, 3441–3454, 1991.

Goossens, M., and J. V. Hollweg, Resonant behaviour of MHD waves on magnetic flux tubes, *Sol. Phys., 145*, 19–44, 1993.

Goossens, M., and M. S. Ruderman, Conservation laws and connection formulae for resonant MHD waves, *Phys. Scr., T60*, 171–184, 1995.

Goossens, M., M. S. Ruderman, and J. V. Hollweg, Dissipative MHD solutions for resonant Alfvén waves in 1-dimensional magnetic tubes, *Sol. Phys., 157*, 75–102, 1995.

Johnson, J. R., and C. Z. Cheng, Kinetic Alfvén waves and plasma transport at the magnetopause, *Geophys. Res. Lett., 24*, 1423–1426, 1997.

Kappraff, J. M., and J. A. Tataronis, Resistive effects on Alfvén wave heating, *J. Plasma Phys., 18*, 209–226, 1977.

LaBelle, J., and R. A. Treumann, Plasma waves at the dayside magnetopause, *Space Sci. Rev., 47*, 175–202, 1988.

Lacombe, C., G. Belmont, D. Hubert, C. C. Harvey, A. Mangeney, C. T. Russell, J. T. Gosling, and S. A. Fuselier, Density and magnetic field fluctuations observed by ISEE 1-2 in the quiet magnetosheath, *Ann. Geophys., 13*, 343–357, 1995.

Mann, I. R., A. N. Wright, and P. S. Cally, Coupling of magnetospheric cavity modes to field line resonances: A study of resonance widths, *J. Geophys. Res., 100*, 19,441–19,456, 1995.

McKenzie, J. F., Hydromagnetic wave interaction with the magnetopause and the bow shock, *Planet. Space Sci., 18*, 1–23, 1970.

Perraut, S., R. Gendrin, P. Robert, and A. Roux, Magnetic pulsations observed onboard GEOS 2 in the ULF range during multiple magnetopause crossings, in *Proceedings of the Magnetospheric Boundary Layers Conference, Alpbach, June 1979, Eur. Space Agency Spec. Publ., ESA SP-148*, 113-122, 1979.

Poedts, S., and W. Kerner, Time scales and efficiency of resonant absorption in periodically driven resistive plasmas, *J. Plasma Phys., 47*, 139–162, 1992.

Poedts, S., M. Goossens, and W. Kerner, Numerical simulation of coronal heating by resonant absorption of Alfvén waves, *Sol. Phys., 123*, 83–115, 1989.

Poedts, S., M. Goossens, and W. Kerner, Temporal evolution of resonant absorption in solar coronal loops, *Comput. Phys. Commun., 59*, 95–103, 1990.

Rezeau, L., A. Morane, S. Perraut, A. Roux, and R. Schmidt, Characterization of Alfvénic fluctuations in the magnetopause boundary layer, *J. Geophys. Res., 94*, 101–110, 1989.

Rezeau, L., A. Roux, and C. T. Russell, Characterization of small-scale structures at the magnetopause from ISEE measurements, *J. Geophys. Res., 98*, 179–186, 1993.

Ruderman, M. S., J. V. Hollweg, and M. Goossens, Nonlinear theory of resonant slow waves in dissipative layers, *Phys. Plasmas, 4*, 75–90, 1997.

Sakurai, T., M. Goossens, and J. V. Hollweg, Resonant behaviour of MHD waves on magnetic flux tubes, I, Connection formulae at the resonant surface, *Sol. Phys., 133*, 227–245, 1991.

Sibeck, D. G., et al., Plasma transfer processes at the magnetopause, *Space Sci. Rev., 88*, 207–283, 1999.

Song, P., C. T. Russell, and C. Y. Huang, Wave properties near the subsolar magnetopause: Pc 1 waves in the sheath transition layer, *J. Geophys. Res., 98*, 5907–5923, 1993.

Southwood, D. J., Some features of field line resonances in the magnetosphere, *Planet. Space Sci., 22*, 483–491, 1974.

Treumann, R. A., J. LaBelle, and T. M. Bauer, Diffusion processes: An observational perspective, in *Physics of the Magnetopause, Geophys. Monogr. Ser.*, vol. 90, edited by P. Song et al., pp. 331–341, AGU, Washington, D. C., 1995.

Wright, A. N., and G. J. Rickard, A numerical study of resonant absorption in a magnetohydrodynamic cavity driven by a broadband spectrum, *Astrophys. J., 444*, 458–470, 1995.

V. Čadež and J. De Keyser, Belgian Institute for Space Aeronomy, Ringlaan 3, B-1180 Brussels, Belgium. (Johan.DeKeyser@bira-iasb.oma.be; Vladimir.Cadez@bira-iasb.oma.be)

(Received December 21, 2000; revised February 20, 2001; accepted March 5, 2001.)